Investigating the Role of Gravity Waves on Mesosphere-Lower-Thermosphere (MLT) Inversions at Low Latitudes

Chalachew Lingerew[1*], U. Jaya Prakash Raju[1]

[1] Department of Physics, Washera Geospace, and Radar Science Laboratory, Bahir Dar University, Bahir Dar, Ethiopia

Correspondence to: Chalachew Lingerew Bizuneh (chalachewlingerew@gmail.com)

Abstract

The Mesosphere and Lower-Thermosphere (MLT) transitional region, encompassing a height range of 60-100 km, is a distinct and highly turbulent zone within the Earth's atmosphere. The region is significant owing to dynamics of atmospheric processes like planetary, tidal, and particularly gravity waves, which contribute to the formation of the Mesospheric Inversion Layer (MIL). Investigating the inversion phenomena is crucial for understanding the dynamics of the middle and upper atmosphere, especially regarding stability and energy transfer. These phenomenons are associated with energy transfer processes, vital for understanding the overall dynamics of the atmosphere. Despite extensive study on an inversion, the formation mechanisms of mesospheric inversions remain poorly understood. Hereunder, the upper and lower inversion phenomena and their causative mechanisms are explored. It utilizes long-term SABER observations during 2005-2020 over the latitude, 3-15° N and longitude, 33-48° E ranges. The results show that the upper inversion occurs more frequently, with a frequency below 40%, compared to the lower inversion, which occurs below 20%. The upper inversion occurs within the height range of 78-91 km, with an inversion amplitude of approximately 20-80 K and a thickness of around 3-12 km. In contrast, the lower inversion is confined to the height range of 70-80 km, with an inversion amplitude of about 10-60 K and a thickness of around 4-10 km. Moreover, the gravity wave indicator potential energy shows high energy (below 100 J/kg) in the upper MLT region (85-90 km) compared to the lower MLT region (70-75 km) with less than 50 J/kg. Considering gravity waves, the Brunt-Väisälä frequency (N^2) stability criteria indicate instability in the upper MLT region with very low values compared to the lower MLT region. This suggests that the high amount of gravity wave potential energy is a consequence of the higher instability in the upper inversion compared to the lower inversion.

Keywords: Mesosphere and Lower Thermosphere (MLT), Upper and Lower Inversions, Perturbed Temperature, Causative Gravity Waves, Potential Energy, Brunt-Väisälä Frequency, Atmospheric Instability.

Introduction

The Mesosphere and Lower-Thermosphere (MLT) region serves as a transitional zone for atmospheric wave processes from the lower and upper atmospheres, including tidal, planetary, and gravity waves. Gravity waves (GWs) originating in the lower atmosphere propagate into the upper mesosphere, where they break and dissipate, releasing energy and momentum. This process influences the thermal structure, global atmospheric circulation, and mesospheric inversion layers (MILs), which are associated with increased temperature variability in mesosphere. MILs indicate wave saturation when the lapse rate falls below the dry adiabatic lapse rate (Sica et al., 2007). Temperature inversions in the mesosphere have been widely observed and studied using various techniques, including lidar, radar, rocket sondes, and satellites, across different geographic locations. Sivakandan et al. (2014) utilized TIMED/SABER kinetic temperature data to examine the occurrence and characteristics of mesospheric inversions over the equatorial Indian region (0 to 10° N and 70 to 90° E) for the years 2002 and 2008. However, they did not explore the causative factors. This study aims to investigate the causes of these inversions, focusing specifically on the role of atmospheric gravity waves.

Gravity waves and mesospheric inversion layers (MILs) are interconnected phenomena within the Earth's atmosphere, particularly in the mesosphere and lower thermosphere (MLT). Inversions are layers within the mesosphere where the temperature profile exhibts an increment. As a result, the temperature increases with altitude, contrary to the typical decrease. These inversion layers often form because of this atmospheric wave dynamic processes, including the breaking and dissipation of gravity waves. As gravity waves propagate upwards, they can grow in amplitude since the atmospheric density decreases with altitude. While these waves reach a critical amplitude, they become broken. This breaking process releases energy and momentum into the surrounding atmosphere, leading to localized heating that creates or enhances mesospheric inversion layers by increasing the temperature with altitude. The breaking of gravity waves contributes to momentum and energy deposition can also generate turbulence, which further influences the structure and instability of an inversion layers.

The deposition of momentum and energy from gravity waves (GWs) is considered a major factor driving large-scale atmospheric circulation, the coupling between atmospheric layers, and the occurrence of inversion phenomena (Fritts and Alexander, 2003; Lindzen, 1981; Smith, 2012). Researchers are also investigating the effects of gravity wave breaking on MLT dynamics to

better understand its role in inversion phenomena, especially in mid- and high-latitude regions (Gan et al., 2012; Walterscheid and Hickey, 2009; Collins et al., 2011; Szewczyk et al., 2013). Observational and modeling studies have examined gravity waves (GWs) as a contributing factor to these inversions (Fritts, 2018; Collins et al., 2014; Sridharan et al., 2008; Ramesh and Sridharan, 2012; Ramesh et al., 2013, 2014, 2017). Despite extensive research, our understanding of how gravity waves influence mesosphere inversions-particularly regarding temperature variability-remains incomplete, even in mid- and high-latitude regions (Singh and Pallamraju, 2018; Fritts et al., 2018). Consequently, studying inversion phenomena and their underlying causes continues to be a crucial area of investigation, especially within MLT dynamics over low-latitude.

Research on the temporal and spatial variability of the mesosphere inversion phenomenon, regarding atmospheric waves, particularly gravity wave activity, is notably lacking in low latitudes. To address this gap, our study investigates the mesosphere inversion phenomenon and its association with gravity wave activity and instability criteria. We use Brunt-Vaisala frequency (N^2) over the low latitudinal band (3°–15° N) with long-term SABER observations from 2005 to 2020. The study is organized as follows: Section 2 details the data and methodology used to analyze the mesosphere inversion phenomenon and their causative gravity waves via the potential energy. Section 3 presents the results, and Section 4 concludes the findings.

2. Observation and Data analysis

2.1 SABER Observation

The TIMED/SABER satellite, launched on December 7, 2001, operates in an elliptical orbit at approximately 625 km altitude with a 74° inclination relative to the equator. Since its launch, SABER has been a crucial tool for atmospheric research, providing extensive data on the middle and upper atmosphere. SABER is a limb-viewing radiometer working in the infrared region (1.27–17 microns) and can measure radiative emissions across a wide range of altitudes. It offers nearly global coverage and continuous 24-hour data over 60 days. The instrument completes 15 orbits daily, each taking about 97 minutes, and collects around 1400 data files per day, with each profile taking 58 seconds. SABER's high-resolution temperature profiles are essential for studying the dynamics and wave processes in the MLT. It provides temperature measurements with an accuracy of 1 to 2 K between 15 and 60 km. The accuracy decreases to 5 K below 85 km and increases to 6.7 K to 10 K near 100 km. This data has been crucial in enhancing our understanding of the thermal structure and dynamic processes in the mesospheric region, as

emphasized by several studies (Garcia et al., 2008; Gan et al., 2012, 2014; Bizuneh et al., 2022; Lingerew et al., 2023; Rezac et al., 2015; Meriwether and Gerrard, 2004; Fechine et al., 2008; Dou et al., 2009; France et al., 2015).

Owing to this, we used the SABER vertical temperature profiles collected within the 60–100 km altitude range. These profiles encompass the period from 2005 to 2020, covering latitudes from 3°N to 15°N and longitudes from 33°E to 48°E. Figure 1 illustrates the monthly mean SABER temperature data for the mesosphere and lower thermosphere. The data aim to illustrate the MLT temperature variability, which helps us identify the inversion layers (MIL). The monthly mean temperatures in the MLT region show a maximum of 200-240 K at altitudes of 60-70 km. Then it decreases to around 160-180 K at 95-100 km throughout the entire period. While the temperature patterns in the 70-90 km altitude range suggest an inversion, these inversions are not visible.

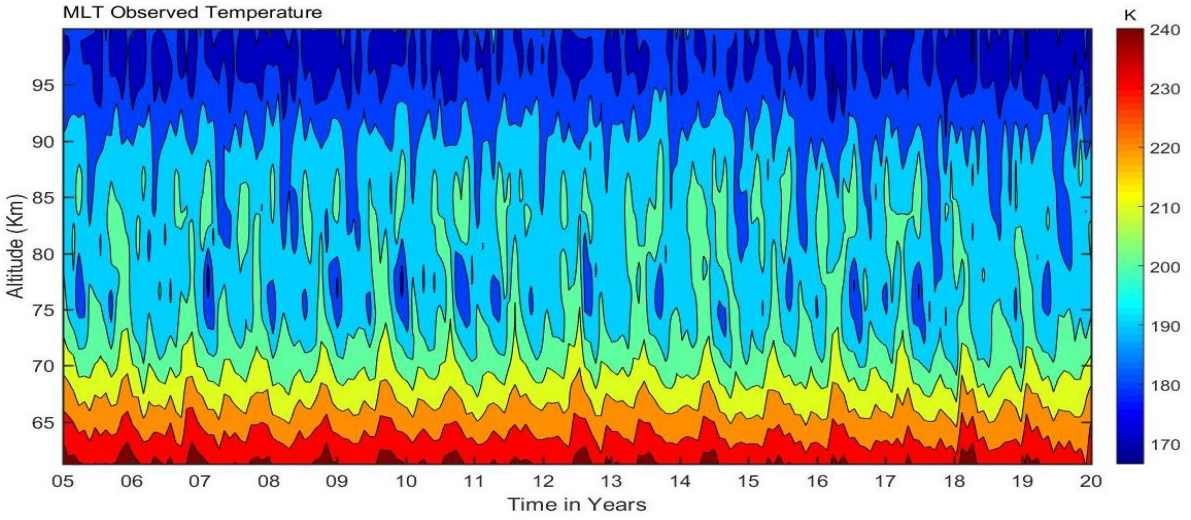

Figure 1. The monthly mean of MLT temperature variability in the height range of 60-100 km during 2005-2020 over the low-latitude.

2.2 Analysis Technique

The Earth's middle atmosphere typically has a negative temperature gradient, but some reports have shown positive temperature gradients in the mesosphere (Meriwether and Gardner, 2000; Gan et al., 2012). This phenomenon, known as the "mesospheric inversion layer (MIL)," is identified using the method described by Leblanc and Hauchecorne (1997) and Fechine et al. (2008). Mesospheric inversions are defined by their thickness (the altitude difference between the maximum warming and cooling) and their amplitude (the temperature difference between

these points) (Meriwether and Gardner, 2000). The following are the criteria for identifying these inversions:

1. The bottom level of the lower inversion is above 70 km, and the top level is below 80 km. For the upper inversion, the bottom level is above 80 km, and the top level is below 92 km.
2. The amplitude is considered larger than 5 K.
3. The thickness is greater than or equal to 3 km.

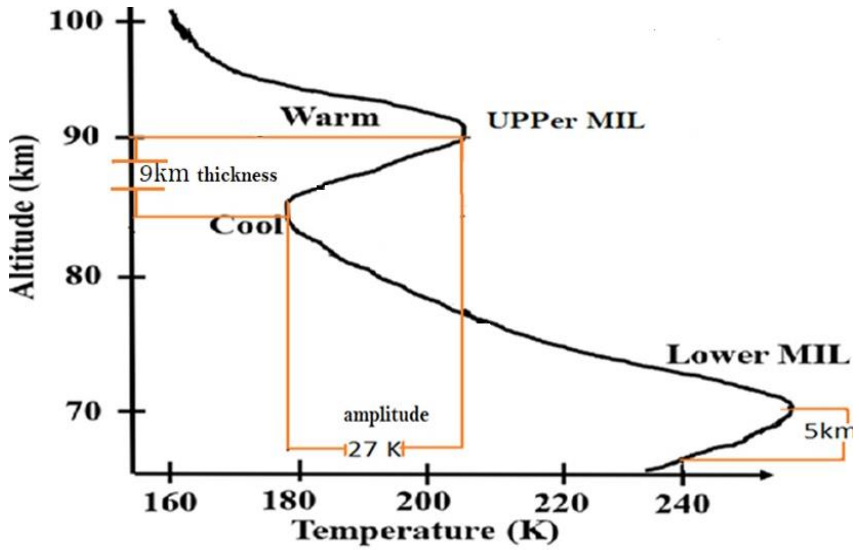

Figure 2. Schematic of upper and lower mesospheric inversion layers shown in the temperature profile for the MLT regions (Adapted from Meriwether and Gerrard, 2004).

Figure 2 illustrates this concept, highlighting the positive temperature difference between the top and bottom levels of the inversion. This method has been widely applied in numerous studies investigating mesospheric inversions (Leblanc et al., 1998; Meriwether and Gardner, 2000; Duck et al., 2001; Duck and Greene, 2004; Cutler et al., 2001; Siva Kumar et al., 2001; Ratnam et al., 2003; Gan et al., 2012). In addition, the frequency of mesospheric inversion layer (MIL) occurrences is determined for the period 2005–2020 in both the upper and lower MLT regions. This frequency is calculated by dividing the number of inversion days in each month by the total number of days in that month over the 16-year observation period (2005–2020).

Mesospheric temperature inversions are linked to MLT instabilities driven by the dynamics of atmospheric wave processes. To identify the causative, short-period atmospheric gravity waves, a high-pass filter with a one-hour interval cutoff frequency is applied using the Brunt-Väisälä

frequency (N2). Another important concept to estimate the Brunt-Vaisala frequency is the potential temperature (θ). It represents the air parcel's temperature when it is displaced adiabatically to a standard pressure level, p_0, from the current pressure level, p. This is based on the first law of thermodynamics.

$$\frac{dT}{T} = \frac{R}{c_p}\frac{dp}{p} \Rightarrow \quad \int_T^0 \frac{dT}{T} = \int_p^{p_0} \frac{R}{c_p}\frac{dp}{p} \qquad (1) \text{ it yields}$$

$$\theta = T\left(\frac{p_0}{p}\right)^{R/c_p} \qquad (2)$$

The vertical motion of an atmospheric air parcel can thus be described by (Liu, 2011; Vadas and Fritts, 2005) as shown in equation (2). This equation calculates the Brunt-Väisälä frequency of the parcel, accounting for the buoyant and gravitational forces acting upon it.

$$\frac{d^2s}{dt^2} = -\mathrm{g}\frac{\rho-\rho_0}{\rho}\, sina \qquad (3)$$

Based on the hydrostatic equation, $\rho = \rho_0$, and $p = p_0 \Rightarrow \frac{\partial p}{\partial z} = \frac{\partial p_0}{\partial z} = -\mathrm{g}\rho_0$ (4) and the ideal gas law, $\rho = p/RT = p_0/RT$ gives the parcels motion of an equation:

$$\frac{d^2s}{dt^2} = -\frac{\mathrm{g}}{\rho}\left(\frac{d\rho}{dp}\frac{\partial p_0}{\partial z} - \frac{\partial \rho_0}{\partial z}\right)z \qquad (5)$$

Following the same approach using the hydrostatic equation (4) and adiabatic equation (6)

$$dln\rho = \frac{dlnp}{\gamma}\ , \gamma = c_p/c_v \qquad (6) \text{ yields}$$

$$\frac{d^2s}{dt^2} = -\frac{\mathrm{g}}{\rho}\left(\frac{\rho}{\gamma p_0}\frac{\partial p_0}{\partial z} - \frac{\partial \rho_0}{\partial z}\right)z = \mathrm{g}\left(\frac{\partial ln\rho_0}{\partial z} - \frac{1}{\gamma}\frac{\partial lnp_0}{\partial z}\right)z \qquad (7)$$

For the ideal gas law of $p = \rho RT$, the natural logarithm is taken for altitude, z on both sides, yielding

$$\frac{\partial ln\rho}{\partial z} = \frac{\partial lnp}{\partial z} - \frac{\partial lnT}{\partial z} \qquad (8)$$

Then after, the potential temperature (θ) of the parcel is calculated as follows based on the equation (2):

$$\frac{\partial ln\theta}{\partial z} = \frac{\partial lnT}{\partial z} - \frac{R}{c_p}\frac{\partial lnp}{\partial z} = \frac{1}{T}\left(\frac{\partial T}{\partial z} + \frac{\mathrm{g}}{c_p}\right) = \left(1 - \frac{R}{c_p}\right)\frac{\partial lnp}{\partial z} - \frac{\partial ln\rho}{\partial z} \qquad (9)$$ to derive the Parcels acceleration based on equations (7) to become:

$$\frac{d^2s}{dt^2} = -\,\mathrm{g}\,\frac{\partial ln\theta_0}{\partial z} z\, sina = -\,\mathrm{g}\,\frac{\partial ln\theta_0}{\partial z} ds.sin^2 a \qquad (10)$$

Whereas by introducing the frequency, N, with $N^2 = \mathrm{g}\,\frac{\partial ln\theta_0}{\partial z}$

The Brunt-Vaisala frequency, N^2 is calculated based on the following mathematical formulation used to characterize atmospheric stability/instability.

$$N^2(z) = \frac{g(z)}{T_0(z)}\left(\frac{\partial T_0(z)}{\partial z} + \Gamma_d\right) \quad (11)$$

Where g is the acceleration due to gravity, N is the Vaisala frequency, T_0 is the background temperature (estimated based on third-order polynomial fitting), $\Gamma_d = {}^{g}/_{c_p}$ is the adiabatic lapse rate, and $c_p = 1004\, J\, K^{-1}\, kg^{-1}$ is the specific heat capacity of the atmosphere at constant pressure. When the Väisälä frequency, N^2, is positive, the atmosphere is stable whereas is negative, the atmosphere is unstable. When the Brunt-Väisälä frequency, N^2, is positive the atmosphere is stable, whereas a negative N^2 indicates atmospheric instability. In this regard, the atmospheric lapse rate, $\Gamma = -\frac{\partial T}{\partial z}$, is larger than the adiabatic lapse rate, ${}^{g}/_{c_p} \approx 9.5\, K\, km^{-1}$. A third-order least squares polynomial fit was applied to the SABER-observed temperature (T) profile to determine the background temperature (T_0), following the method outlined by Leblanc and Hauchecorne (1997). subsequently the perturbed temperature (Tp) is computed by subtracting the background temperature from the observed temperature data (T) in equation (12),

$$T_p' = T - T_0 \quad (12)$$

After estimating the perturbed temperature (Tp), a high-pass band filter is applied. This filter removes low-frequency components associated with planetary and tidal waves, retaining the high-frequency components related to short-period gravity waves (John and Kumar, 2012). This process isolates the influence of gravity waves, enabling accurate calculation of their potential energy. The high-pass filter operates within known frequency ranges, typically below a one-hour period.

$$E_p(z) = \frac{1}{2}\left(\frac{g(z)}{N(z)}\right)^2\left(\frac{T_p'(z)}{T_0(z)}\right)^2 \quad (13)$$

The potential energy of the waves, a function of altitude (z), is used to determine the impact of atmospheric gravity waves on atmospheric inversions.

3. Results and discussion

3.1 Identification and Characteristics of the Lower and Upper MLT Inversion

The SABER temperature profiles, covering altitudes of 60–100 km during 2005 to 2020, are shown in the contour plots of Figure 3. Figures 3(a and b) depict the upper MLT (mesospheric and lower thermospheric), while Figures 3(c and d) show the lower MLT region. The first

horizontal panel of Figures 3(a) and 3(c) show observed temperatures ranging from approximately 180–220 K, before accounting for inversion layers. Whereas, the second horizontal panel of Figures 3(b) and 3(d) show inversion day temperatures, ranging from 180–225 K.

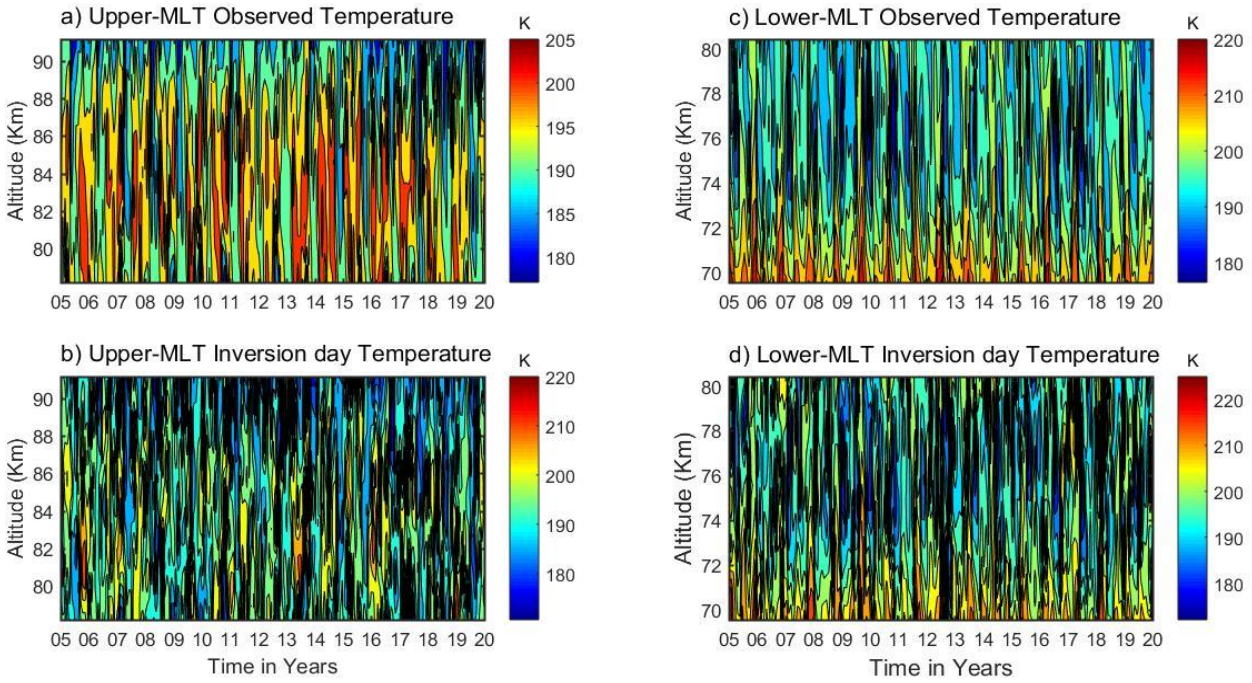

Figure 3. The upper and lower mesosphere observed temperatures in the first horizontal panel at (a and c) with their inversions in the second horizontal panel at (b and d).

The upper left panel of Figure 3(a) shows the observed temperature in the upper mesosphere ranges from approximately 180–205 K at altitudes of around 80–90 km. The upper right panel of Figure 3(c) shows the lower mesosphere, with temperatures ranging from about 180–220 K at altitudes of approximately 70–80 km. In contrast, the lower left panel of Figure 3(b) shows an upper-mesosphere inversion day temperature ranges from 180–220 K at an altitude of approximately 80–90 km. The lower right panel of Figure 3(d) shows a lower-mesosphere inversion day temperature, with the temperature ranging from 180–225 K at an altitude of approximately 70–80 km. These inversion day temperatures are higher than those shown in Figures 3(a) and 3(c). This indicates that maximum temperatures occur on inversion days in both the upper and lower MLT regions relative to the observed temperature. These inversion day temperatures in Figures 3(b) and 3(d) suggest a temperature gradient shifting from negative to positive. This could be due to factors such as atmospheric waves (planetary, tidal and particularly gravity waves), chemical reactions, or solar radiation. Our temperature observations for the lower MLT region on an inversion day, within the altitudinal range of 70–80 km, align with

those reported by Sivakumar et al. (2001), who identified inversion day temperature variability in the altitudinal range of 73–79 km. Additionally, Sivakandan et al. (2014) examined mesospheric inversions in the 60–105 km altitude range over low-latitude regions; their findings closely match our results.

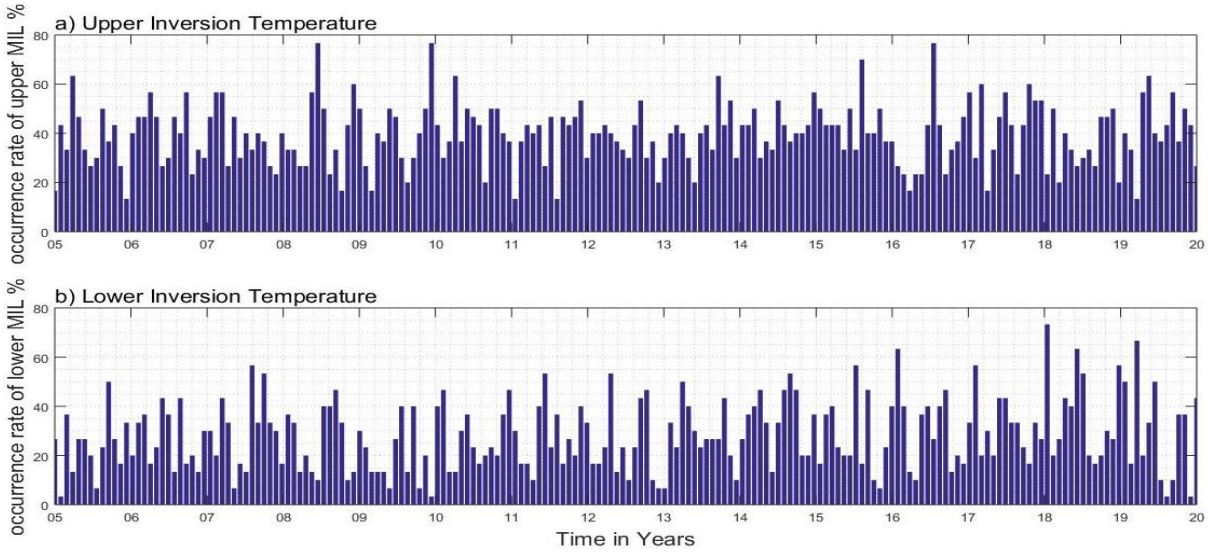

Figure 4. The frequency occurrence rate (percentage) of the (a) upper and (b) lower inversion temperatures during 2005-2020 over low latitudes.

Figure 4 shows the frequency occurrence rate of mesospheric inversion layers (MILs) in histograms. Figure 4(a) shows the occurrence rate for upper MILs, while Figure 4(b) shows the rate for lower MILs. The mean frequency occurrence rate of upper inversions is approximately below 40%. Peak rates range from 60% to 78%, notably in the years 2008, 2010, and mid-2016. In contrast, the mean occurrence rate for lower inversions of Figure 4(b) is approximately below 20%. The overall occurrence rate for upper inversions is relatively higher compared to lower inversions; this may be related to atmospheric wave activities, mainly gravity waves. Hauchecorne et al. (1987) and France et al. (2015) discuss the effects of gravity waves on inversion variability in the upper and lower mesosphere. Regarding these findings, Figure 5 examines the characteristics of the inversion day temperature variability, based on their amplitude and thickness. It focuses on base height, amplitude, and thickness, before examining the effects of gravity waves on an inversion. Histograms display the frequency distribution of amplitude, thickness, and base height for MLT temperature variability on inversion days, with best-fit Gaussian distribution curves shown in red. The observed distributions align with Gaussian curves, indicating that the number of mesospheric inversion layers (MILs) follows a normal distribution. This suggests that the attributes are real-valued random variables. The left column has three rows showing histograms of (a) amplitude, (b) thickness, and (c) base height of

the inversion day temperature variability for the upper MLT. These histograms also include the statistical metrics mean and standard deviations (SD) with their values. The corresponding right column has three rows representing (d) amplitude, (e) thickness, and (f) base height of the inversion day temperature variability for the lower MLT region.

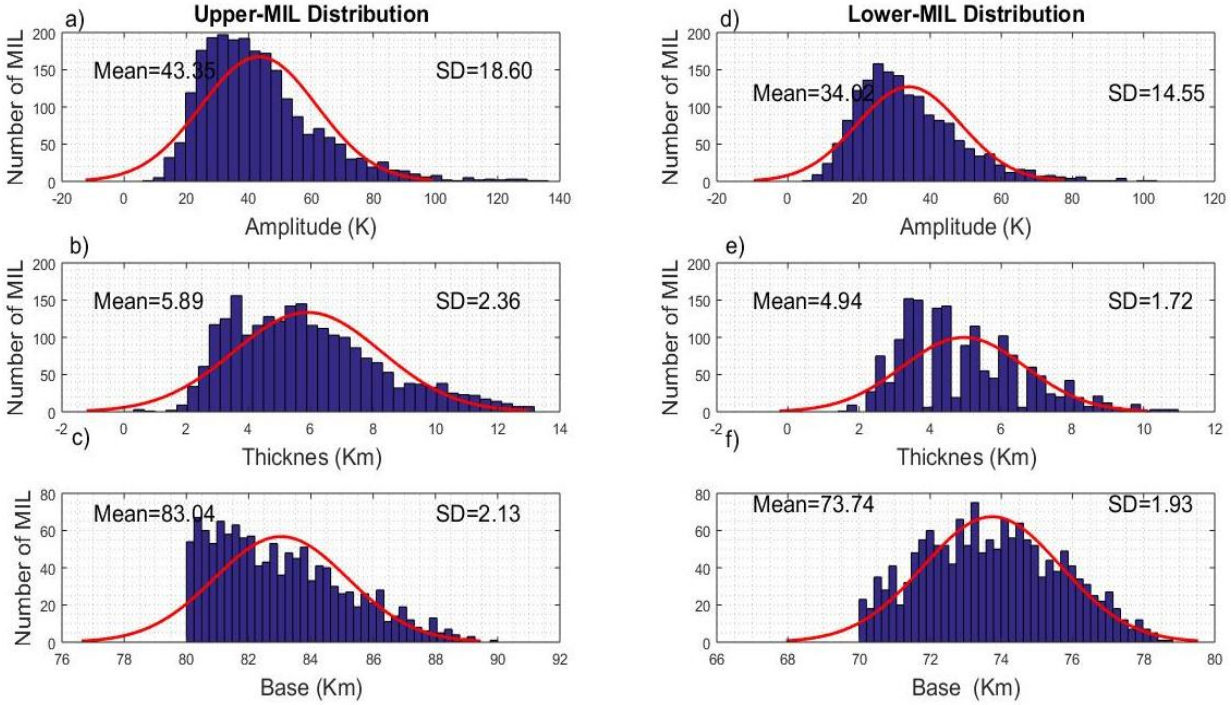

Figure 5. The histograms depict the occurrence of MLT inversion day temperature variability. The first vertical panel shows the distribution of (a) amplitude, (b) thickness, and (c) base height for the upper inversion day. The second vertical panel presents the corresponding distribution for the lower inversion, including (d) amplitude, (e) thickness, and (f) base height.

The amplitude of upper inversion day temperature variability in Figure 5(a) ranges between 20 and 80 K, with a peak value of 38 K. This follows a Gaussian distribution with a large standard deviation (SD) of 18.6, which idicates high inversions. The thickness of the inversion layer for upper MILs, shown in Figure 5(b), ranges from 3 to 9 K, and their most probable value is 5.5 K, with a low SD of 2.3. The base height of the upper MIL in Figure 5(c) spans from ~80 to 90 km, with a peak value of around 83 km. This indicates a large number of upper MLT inversions, with an SD of 2.13. The highest number of upper inversions between 2005 and 2020 is observed at 82 km. This may be attributed to gravity wave breaking and energy dissipation, influenced by waves generated from lower atmospheric regions and solar flux impacts.

The lower inversion amplitude, shown in Figure 5(d), ranges from 10 to 60 K, with a peak value of 25 K and a standard deviation (SD) of 14.5. The inversion thickness, as illustrated in Figure 5(e), spans 3 to 8 km, with the most likely value at 3.8 km and a low SD of 1.72. The base height of the lower inversion in Figure 5(f) ranges from 70 to 80 km, with a peak value of around 74 km and a lower SD of 1.93. Previous investigations by Sivakandan et al. (2014) from the Indian sector reported amplitudes ranging from 14–39 K in 2002 and 15–42 K in 2008. The thicknesses ranged between 2.7–7.5 km in 2002 and 2.8–7.3 km in 2008, under the influence of solar flux. These findings align well with the present study, indicating no significant variation in characterizing mesospheric inversion based on amplitude and thickness in the low-latitude region within the altitude range of 60 to 90 km.

3.2 Latitudinal Variations of Mesospheric Inversion Layers (MILs)

This section examines the spatiotemporal variability of upper and lower mesosphere inversion phenomena. Contour plots of time vs. latitude in Figures 6 and 7 show the variability of upper and lower MLT inversion amplitude, thickness, and base height over the low-latitude band (3-15°) during 2005–2020. The upper inversion is observed around 80–90 km; their maximum amplitude, in the range of 90–120 K, occurs over latitude bands (5-12°) during 2005, 2007, mid-2011, 2013, 2015, 2016, mid-2019, and 2020 (Figure 6(a)). The second horizontal panel of Figure 6(b) shows the thickness, with a maximum range of ~(8–12 km) across the entire latitudinal region (3-15° N). The third horizontal panel of Figure 6(c) shows the base height, with relative maximum values around ~(84-88 km), in the latitudinal range between (4° & 14°) N during 2006, 2008, 2010, 2012, 2016, and 2018.

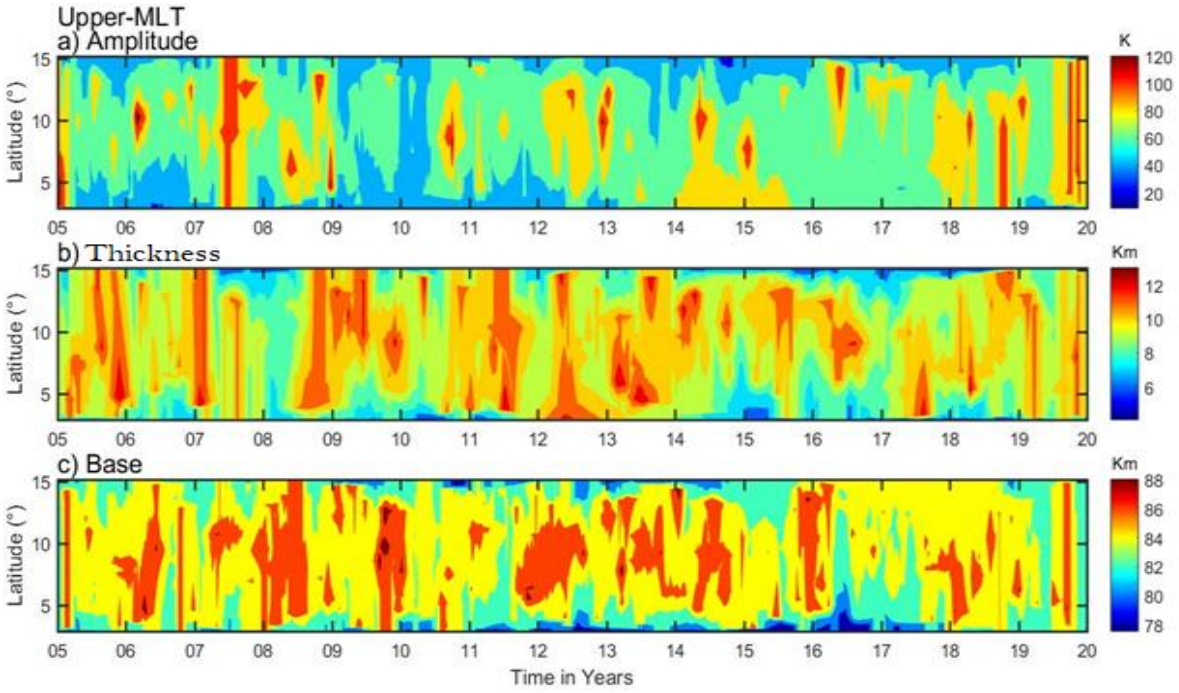

Figure 6. The daily upper inversions (~80-90 km) of (a) amplitude, (b) thickness, and (c) base height during 2005-2020 over latitudinal variation.

Whereas, the contour plots of Figure 7(a, b, and c) show the lower inversions (MILs) amplitude, thickness, and base height over an altitudinal range of ~70-80 km, respectively. Overall, amplitude values ranged from approximately 30-60 K across all latitudinal bands, reaching peak ranges of about 80-100 K during 2013, 2015, 2016, and 2019 in various latitude regions between 5° and 14°N. The second horizontal panel of Figure 7(b) indicates thickness values ranging from 5-7 km across the entire latitude band, with maximum thickness reaching 8-10 km in 2012-2013, 2016, and 2019. The final horizontal panel of Figure 7(c) shows a base height of 76–80 km across most latitudes and periods, with notable exceptions in 2008, 2014, and mid-2018, where the base height reaches its maximum.

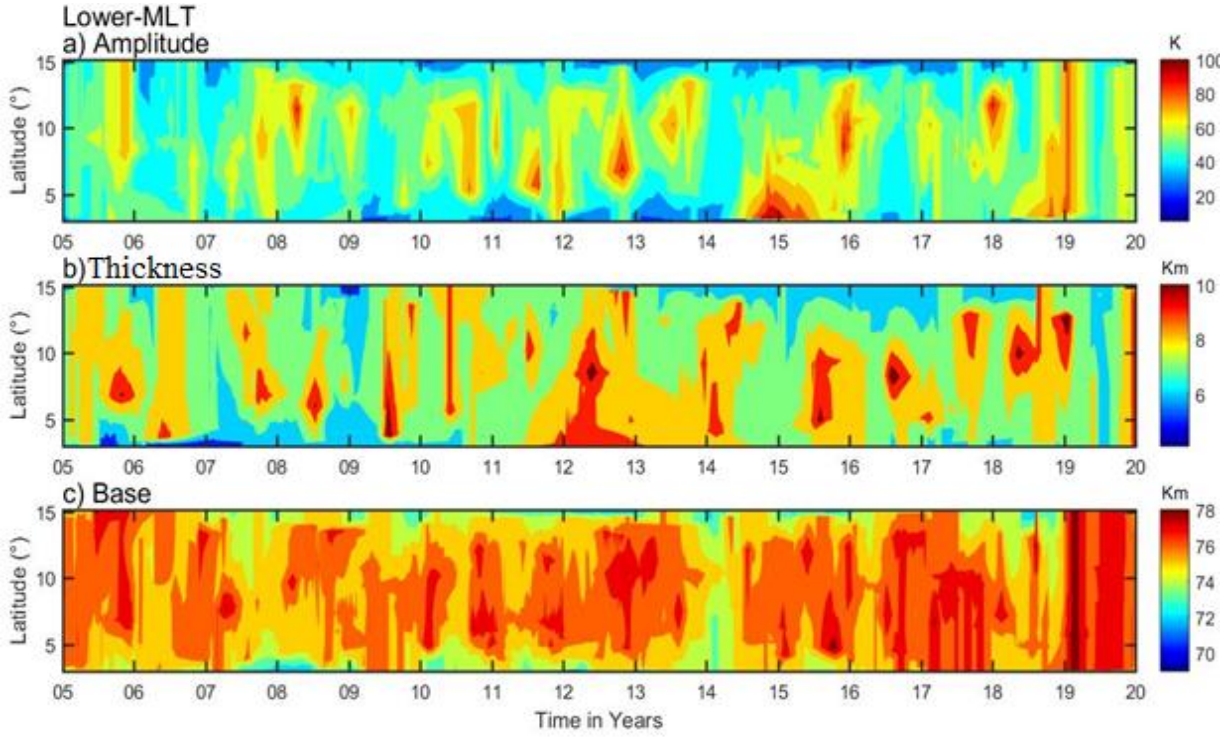

Figure 7. Same as Figure 5, but for the lower mesosphere inversions (~70- 80 km).

The higher amplitude and thickness are demonstrated in the upper and lower inversion to exhibit a suggested highly dynamic phenomenon. These valuable investigations are confirmed in Gan et al. (2012) based on SABER satellite observation at low latitudes.

3.3 Analysis of Perturbed Temperature Variations in the MLT Region

The perturbed temperature (T_p) of the upper and lower MLT inversions in Figure 8 and 9 can further be used to calculate their derived potential energy of gravity waves and the Brunt-Väisälä frequencies (N^2). First, the upper inversion profiles are identified in the MLT region during the entire observational period of 2005-2020, as displayed in the contour plot of Figure 8(a). Based on the observed temperature, which ranges from ~170 to 220 K with minimal variability, the background temperature is estimated. A 3rd-order polynomial fit is applied to calculate the background temperature (T_0), as shown in the contour plot of Figure 8(b). This maximum background temperature exhibits a periodic variability over an altitude of around ~82-87 km, ranging from ~195-197 K. The perturbed temperature profiles (Tp), determined by subtracting the background temperature profiles (To) from the observed inversion temperature (T), are in the range between -25 and +25 K, as illustrated in Figure 8(c).

The lower-MLT region perturbed temperature (Tp) is calculated using the same approach as the upper-MLT perturebed temperature, using the observed and background temperatures. Their corresponding contours are displayed in Figure 9(a-c).

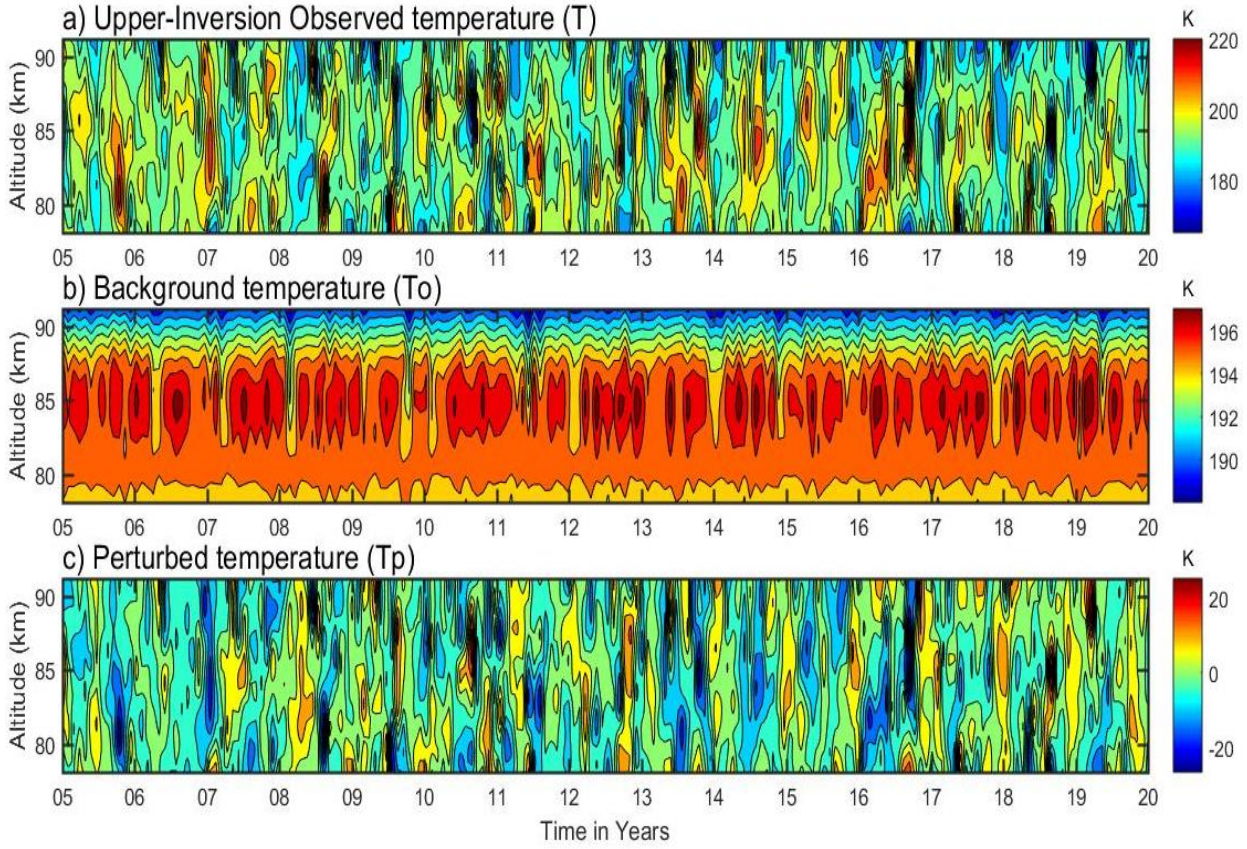

Figure 8. The upper mesosphere temperatures in the vertical panel are: (a) inversion day observed temperature; (b) background temperature; and (c) perturbed temperature in the upper mesosphere region.

In Figure 9(a), the observed temperature of the lower inversion ranges from ~170-220 K. Whereas, the background temperature of the lower inversion ranges from ~ 195-210 K, with maximum values of ~200-210 K at a height of ~70-72 Km, as shown in Figure 9(b). The derived lower-MLT perturbed temperature from the observed and background temperature is presented in Figure 9(c) and ranges from -25 to 20 K. Notably, the upper-MLT perturbed temperature is at its maximum compared to the lower-MLT region, possibly due to a highly dynamic phenomenon.

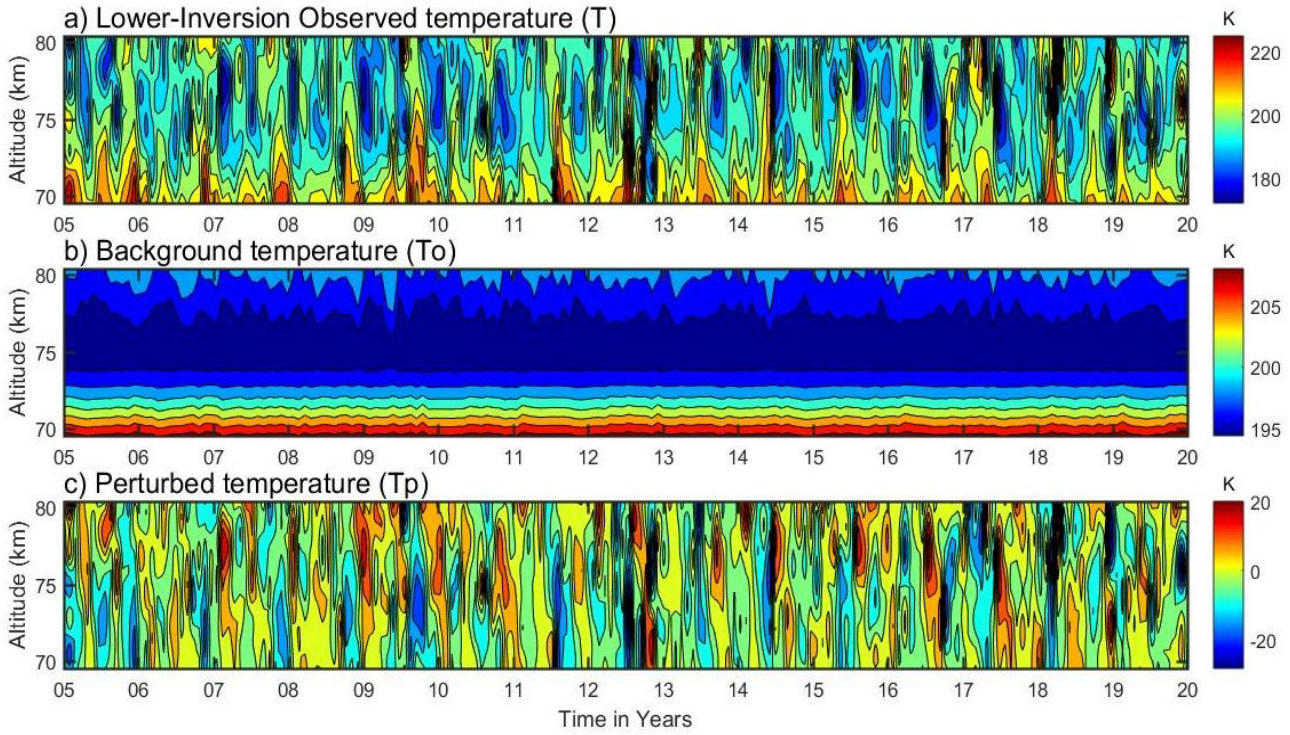

Figure 9. Same as Figure 7, but for the lower mesosphere atmospheric region.

3.4 Effects of Gravity Waves on Mesosphere Inversions and Associated Instability

Atmospheric gravity waves form when air parcels are oscillated due to the restoring force of gravity after being transported vertically. Several factors contribute to these waves, including airflow over mountains, convection, and wind shear. As the waves propagate vertically, they break and dissipate, releasing energy and momentum into the surrounding atmosphere, which contributes to the formation of inversion layers. The gravity wave contribution is quantified by calculating the potential energy and assessing their impact on MLT instability through the Brunt-Väisälä frequency (N^2), derived from perturbed temperature (Tp') data spanning 2005–2020. Several authors (Tsuda et al., 2000; Wang and Geller, 2003; Liu et al., 2014; Thurairajah et al., 2014) suggest that gravity wave activity is represented by potential energy. Further investigation is required, focusing on altitudes of 90, 85, 75, and 70 km, to evaluate the impacts of gravity waves on an inversion by applying a high-pass filter with a one-hour interval to the Tp' data (see Figure 10 a-d). The high-pass filter attenuates low-frequency components, removing the effects of long-period wave oscillations, such as tidal and planetary wave contributions. This effectively isolates the gravity waves (Gw), allowing a clearer focus on their impact on MLT inversions, as appeared in Figure 10.

The blue curve in Figure 10(a to d) appears smoother after applying the high-pass filter to the perturbed temperature. However, the filter removes the peaks of low-frequency variations,

resulting in retained perturbed temperature values that appear more uniform, creating a smooth plateau effect. In the upper mesosphere (90 and 85 km), the filter reduces the amplitude of wave oscillations from approximately ±20 K to ±10 K, as shown from the blue curve in Figure 10a and b, compared to the red curve. Similarly, in the lower mesosphere (75 and 70 km) at (Figure 10 c & d) the amplitude decreases from ~(-20 to 20 K) to ~(-8 to 8 K) by filtering out higher amplitudes.

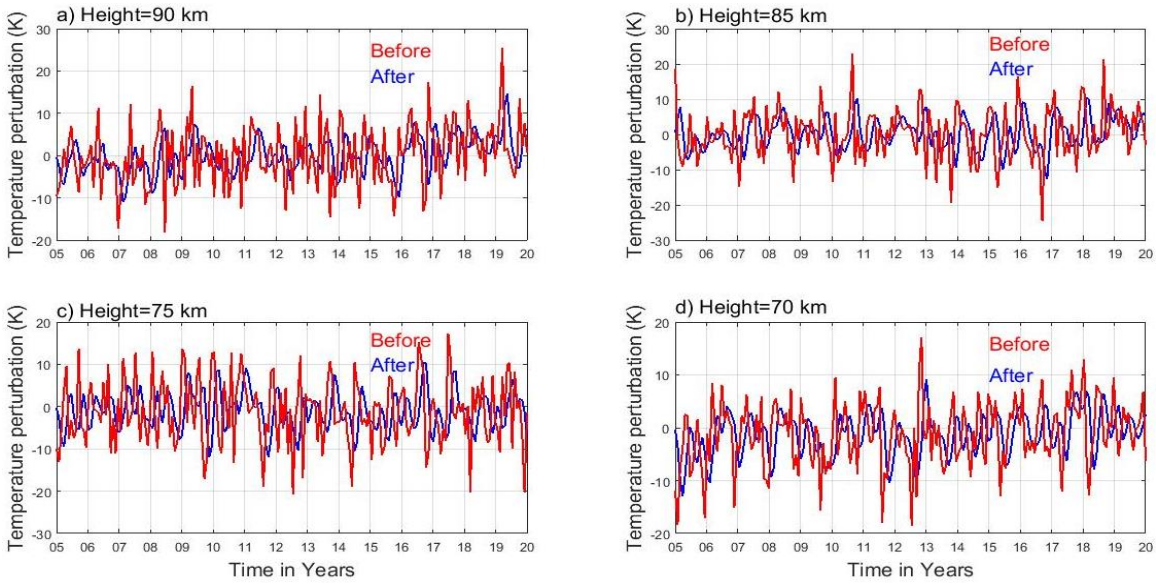

Figure 10. Perturbed temperature profiles before (red color) and after (blue color) applying the high-pass filter for the upper (90 and 85 km) and lower (75 and 70 km) regions.

In the MLT atmospheric region, gravity wave breaking typically dissipates their potential and kinetic energy, leading to increased turbulence and mixing. As illustrated, gravity wave propagation and dissipation are major forces in the MLT (Lindzen, 1981; Holton, 1983), influencing the middle and upper atmospheric regions. This has a substantial impact on the overall dynamics as well as the MLT's thermal structure, particularly the increase in temperature variability with elevation, known as inversion. Holton et al. (2003) and Holton and Hakim (2013) has demonstrated an interaction between the potential energy of gravity waves and inversions. This notable upper and lower inversions are observed in Figure 4 during the period 2005–2020 over the low-latitude regions. During this period, particularly for the upper-MLT region above 80 km altitude, high-resolution SABER satellite temperature data revealed the presence of a strong mesospheric inversion layer (MIL), with peak occurrence rates ranging between 60% and 78%, especially during 2010, 2014, 2016/17, and 2018/19, Figure 4a. Correspondingly, at the same time and in the same region (upper-MLT), at altitudes of 85 and 90 km, there is a noticeable increase in gravity wave potential energy (Ep), shown in Figure 11. The

maximum potential energy (PE) for the upper-MLT region corresponds to the breaking or dissipation of gravity waves as they propagate upward. This spike in potential energy coincides with the occurrence of the inversion layer, suggesting that the breaking or dissipation of gravity waves releases energy into the atmosphere, contributing to localize heating in the mesosphere and leading to the formation of the inversion. The sudden transfer of momentum and energy from the breaking GWs to the surrounding atmosphere disrupts the thermal structure, causing the temperature inversion. In this case, the temporal and spatial coincidence between the peak in gravity wave potential energy and the formation of the inversion demonstrates a clear physical connection. The energy released from breaking GWs plays a direct role in the creation of the inversion layer, as shown in Figures 4 and 11. Similarly, the statistical distributions of upper-MLT inversions in Figure 5(a) show maximum amplitudes, which correspond to the maximum potential energy of gravity waves in Figure 11(a & b). This provides a straightforward demonstration of how gravity wave dynamics-specifically, the dissipation of their potential energy-are linked to the formation of mesospheric inversion layers (MILs).

Figure 11 (a-d) demonstrates that the spatiotemporal variability of gravity wave potential energy, showing over the upper-MLT at (90 and 85 km) and the lower-MLT at (75 and 70 km). Figure 11(a) of upper-MLT inversions at 90 km shows maximum gravity wave potential energies, ranging from ~70 to 90 J/kg, over the longitudinal regions of 45-47° E, as well as at 43° E, and 44° E during 2011, 2017, and 2019. In contrast, potential energies being the least in amount around ~10 to 60 J/kg are present across the entire longitudinal region from 33-48° E. Figure 11(b) of upper-MLT region shows maximum potential energies of ~70 to 100 J/kg over the longitudinal regions of 34°, 44°, and 46° E during 2014, 2016, and 2018 at 85 km. Its minimum potential energies between 20 and 70 J/kg appear over the longitude regions from 33-48° E. Whereas, Figures 11(c) and 11(d) depict the gravity wave potential energy in the lower-MLT regions at 75 and 70 km, respectively. At 75 km, Figure 11(c) shows a relative maximum potential energy of 40-50 J/kg over the longitudinal regions of 46°, 42°, 40°, 37°, 36°, and 38° E during 2011, 2012, 2017, 2013–2015, 2018, and 2020. Similarly, Figure 11(d) illustrates gravity wave potential energy ranging from 2-30 J/kg at 70 km across the longitudinal region of 33-48° E. Their maximum potential energy of 25-30 J/kg is observed in certain longitudinal regions over time.

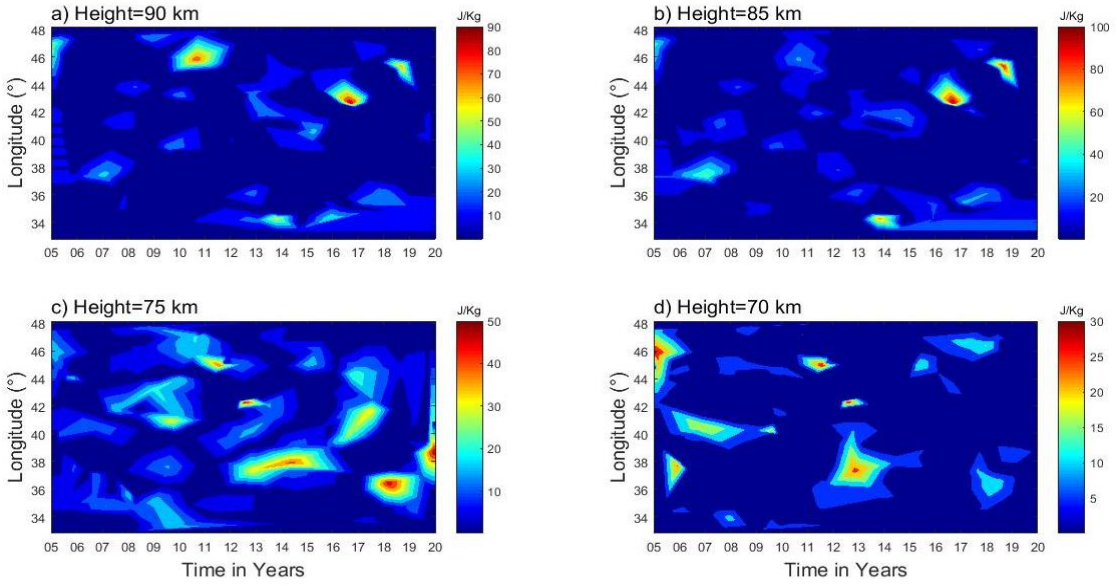

Figure 11. Gravity wave potential energy for the upper (90 and 85 km) and lower (75 and 70 km) MLT regions.

The role of gravity waves in the MLT region instability, the Brunt-Väisälä frequency is analysised. Contour plots in Figure 12 (a-d) show the spatiotemporal variability of the Brunt-Väisälä frequency, with Figures 12(a and b) representing the upper-MLT (90 and 85 km) and Figures 12(c and d) representing the lower-MLT (75 and 70 km). The Brunt-Väisälä frequency (N^2) shows that the upper MLT region is more unstable (~0.027 at 90 km and ~0.029 at 85 km) relative to that of the lower MLT region (~0.033 at 75 km and ~0.035 at 70 km). These different values of brunt-vaisala frequency under a quencyquence of gravity waves generation in different sizes, with smaller waves being the main derivers of instability and turbulence in the MLT (mesosphere and lower thermosphere) region (Liu and Meriwether, 2004; Szewczyk et al., 2013). Hauchecorne et al. (1987) proposed a model where a series of breaking gravity waves leads to the formation of MILs through the gradual accumulation of heat, which contributes to instability. Conducting mesospheric inversion layer (MIL) phenomena is crucial for understanding MLT atmospheric dynamics, especially when it comes to stability and energy transfer.

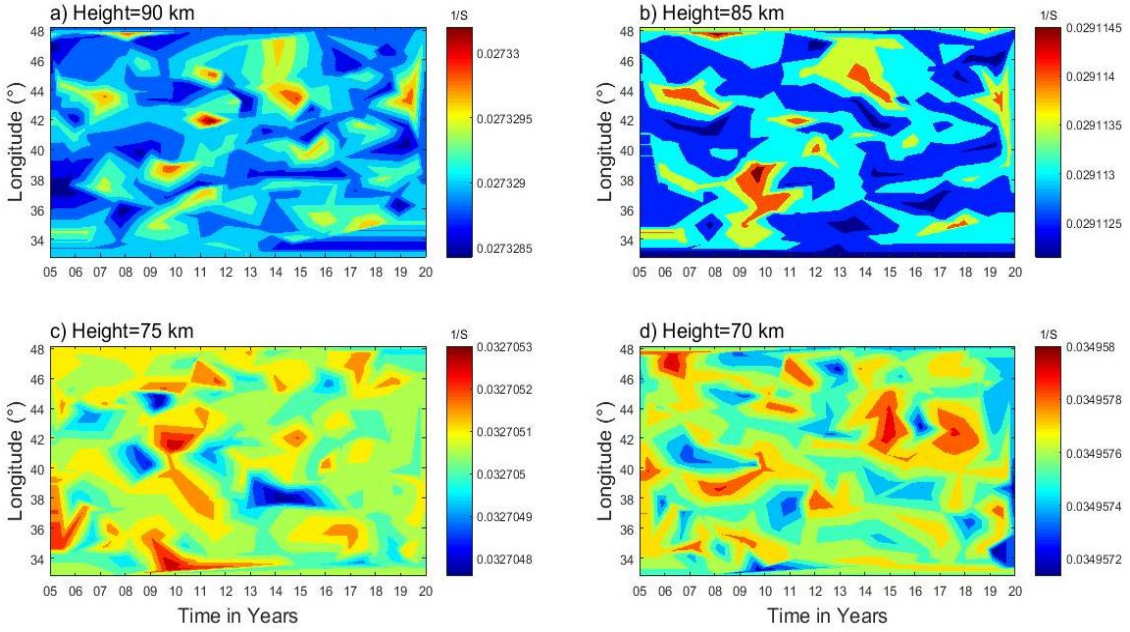

Figure 12. Brunt-Väisälä frequency (N^2) variability for the upper (90 and 85 km) and lower (75 and 70 km) MLT regions.

4 Summary

In this article, 16 years of SABER MLT temperature profiles are utilized to investigate the MIL phenomenon and its causative mechanism through gravity wave potential energy (P_E) and instability criteria of Brunt-Väisälä frequency (N^2) over low-latitudes. The following conclusions are drawn from the observations in this article:

- ✓ The upper mesosphere inversion frequency occurs more often than the lower mesosphere inversion.
- ✓ Analysis of the MIL characteristic features reveals the most probable values for the upper inversion: amplitude of 38 k, thickness of 5.5 km, and base height of 78 km. The lower inversion has an amplitude of 25 K, a thickness of 3.8 km, and a base height of 73 km.
- ✓ The upper mesosphere region has higher gravity wave potential energy compared to the lower mesosphere region.
- ✓ The high potential energy in the upper mesosphere region is likely due to the deposition of energy and momentum by gravity wave breaking. This could influence the dynamics of the inversion phenomenon.
- ✓ The Brunt-Väisälä frequency (N^2) indicates that the upper mesosphere region is less stable than the lower mesosphere region. This lower stability contributes to the high potential energy in the upper mesosphere, which leads to larger inversion phenomena.

✓ Atmospheric processes vary significantly from region to region, with altitude, and over time.

D***ata availability.*** The SABER data are freely available via the link at http://saber.gats-inc.com/index.php.

Author contribution. Chalachew Lingerew: data curation, investigation, software, visualization, writing the original draft, and writing review. U. Jaya Prakash Raju; supervision, and editing.

Competing interest. The authors declare that they have no conflict of interest relevant to this study.

Acknowledgments. The Authors would like to express their gratitude to the National Aeronautics and Space Administration (NASA) for providing the SABER data from the website: http://saber.gats-inc.com/index.php.

References

Begue, N., Mbatha, N., Bencherif, H., Loua, R. T., Siva Kumar, V., & Leblanc, T.: Statistical analysis of the mesospheric inversion layers over two symmetrical tropical sites: Reunion (20.8° S, 55.5° E) and Mauna Loa (19.5° N, 155.6° W). *In Annales Geophysicae*, 35, 1177-1194, 2017.

Bizuneh, C.L., Prakash, R., and Nigussie, M.: Long-term temperature and ozone response to natural drivers in the mesospheric region using 16 years (2005–2020) of TIMED/SABER observation data at 5-15^{0}N. Advances in Space Research, 70, 2095–2111, https://doi.org/10.1016/j.asr.2022. 06.051, 2022.

Collins, R. L., Lehmacher, G. A., Larsen, M. F., and Mizutani, K.: Estimates of vertical eddy diffusivity in the upper mesosphere in the presence of a mesospheric inversion layer, Ann. Geophys., 29(11), 2019–2029, http://doi:10.5194/angeo-29-2019-2011, 2011.

Cutler, L. J., Collins, R. L., Mizutani, K., and Itabe, T.: Rayleigh lidar observations of mesospheric inversion layers at Poker Flat, Alaska (65^0 N, 14^0 W), Geophys. Res. Lett., 28, 1467–1470, https://doi.org/10.1029/2000GL012535, 2001.

Dou, X., Li, T., Xu, J., Liu, H. L., Xue, X., Wang, S., Leblanc, T., McDermid, I. S., Hauchecorne, A., Keckhut, P., Bencherif, H., Heinselman, C., Steinbrecht, W., Mlynczak, M. G., and Russell III, J. M.: Seasonal oscillations of middle atmosphere temperature observed by Rayleigh lidars and their comparisons with TIMED/SABER observations, J. Geophys. Res., 114, D20103, https://doi.org/10.1029/2008JD011654, 2009.

Duck, T. J., Sipler, D. P., and Salah, J. E.: Rayleigh lidar observations of a mesospheric inversion layer during night and day, Geophys. Res. Lett., 28, 3597–3600, 2001.

Duck, T. J. and Greene, M. D.: High Arctic observations of mesospheric inversion layers, Geophys. Res. Lett., 31, L02105, https://doi.org/10.1029/2003GL018481, 2004.

Eckermann, S.D., Hirota, I., and Hocking, W. K.: Gravity wave and equatorial wave morphology of the stratosphere derived from long-term rocket soundings. Q. J. R. Meteorol. Soc., 121, 149 186, http://doi.org/10.1002/qj.49712152108, 1994.

Emanuel, K.A.: Atmospheric Convection, Oxford University Press, New York, 580pp, 1994.

Fechine, J., Wrasse, C. M., Takahashi, H., Mlynczak, M. G., and Russell, J. M.: Lower-mesospheric inversion layers over Brazilian equatorial region using TIMED/SABER temperature profiles, Adv. Space Res., 41, 1447–1453, https://doi.org/10.1016/j.asr.2007. 04.070, 2008.

Fritts, D. C., Wang, L., Laughman, B., Lund, T. S., & Collins, R. L.: Gravity wave dynamics in a mesospheric inversion layer: 2. Instabilities, turbulence, fluxes, and mixing. Journal of Geophysical Research: Atmospheres, 123, 649–670, https://doi.org/10.1002/2017JD027442, 2018.

France, J. A., Harvey, V. L., Randall, C. E., Collins, R. L., Smith, A. K., Peck, E. D., and Fang, X.: A climatology of planetary wave-driven mesospheric inversion layers in the extratropical winter, J. Geophys. Res.-Atmos., 120, 399–413, https://doi.org/10.1002/2014JD022244, 2015.

Fritts, D. C., and Alexander, M. J.: Gravity wave dynamics and effects in the middle atmosphere, Rev. Geophys., 41, 1003, https://doi.org/10.1029/2001RG000106, 2003.

Fritts, D. C., Laughman, B., Wang, L., Lund, T. S., & Collins, R. L.: Gravity wave dynamics in a mesospheric inversion layer: 1. Reflection, trapping, and instability dynamics. Journal of Geophysical Research: Atmospheres, 123, 626-648, https://doi.org/10.1002/2017JD027440, 2018.

Gan, Q., Zhang, S. D., and Yi, F.: TIMED/SABER observations of lower mesospheric inversion layers at low and middle latitudes, J. Geophys. Res., 117, D07109, https://doi:0.1029/2012JD 017455, 2012.

Garcia-Comas, M., Lopez-Puertas, M., Marshall, B. T., Winter Steiner, P. P., Funke, B., Bermejo-Pantaleon, D., Mertens, C. J., Remsberg, E. E., Gordley, L. L., Mlynczak, M. G., and Russell III, J. M.: Errors in Sounding of the Atmosphere using Broadband Emission Radiometry (SABER) kinetic temperature caused by non-local-thermodynamic-equilibrium model parameters, J. Geophys. Res., 113, D24106, doi: 10.1029/2008JD010105, 2008.

Hirota, I.: Climatology of gravity waves in the middle atmosphere. J. Atmos. Terr. Phys., 46, 767–773, http://doi.org/10.2151/jmsj1965.63.6-1055, 1984.

Hamilton, K.: Climatological Statistics of Stratospheric Inertia-Gravity Waves Deduced from Historical Rocket-sonde Wind and Temperature Data. J. Geophys. Res., 96, 20831–20839, http://doi.org/10.1029/91JD02188, 1991.

Hauchecorne, A., Chanin, M. L., & Wilson, R.: Mesospheric temperature inversion and gravity wave breaking. *Geophysical Research Letters*, 14(9), 933-936, https://doi.org/10.1029/GL014i009p00933, 1987.

Holton, J. R., Curry, J. A., and Pyle, J. A.: *Encyclopedia of atmospheric sciences*, volume 1. Academic Press, 2003.

Holton, J. R.: The influence of gravity wave breaking on the general circulation of the middle atmosphere, J. Atmos. Sci., 40, 2497–2507, 1983.

Holton, J. R. and Hakim, G. J.: *An introduction to dynamic meteorology*. Academic Press, 2013.

Irving, B. K., Collins, R. L., Lieberman, R. S., Thurairajah, B., and Mizutani, K.: Mesospheric Inversion Layers at Chatanika, Alaska (65°N, 147°W): Rayleigh lidar observations and analysis, J. Geophys. Res. Atmos., 119, 11,235–249, http://doi:10.1002/2014JD021838, 2014.

John, S.R., Kumar, K. K.: TIMED/SABER observations of global gravity wave climatology and their interannual variability from stratosphere to mesosphere lower thermosphere. Clim. Dyn., 39, 1489–1505, http://doi.org/10.1007/s00382-012-1329-9, 2012.

Leblanc, T., McDermid, I. S., Hauchecorne, A., and Keck hut, P.: Evaluation of optimization of lidar temperature analysis algorithms using simulated data, J. Geophys. Res., 103, 6177–6187, 1998.

Leblanc, T., and Hauchecorne, A.: Recent observations of mesospheric temperature inversions, J. Geophys. Res., 102, 19471–19482, https://doi.org/10.1029/97JD01445, 1997.

Lindzen, R. S.: Turbulence and stress due to gravity waves and tidal breakdown, J. Geophys. Res., 86, 9707–9714, https://doi:10.1029/JC086iC10p09707, 1981.

Lingerew, C., Jaya Prakash Raju, U., & Guimarães Santos, C. A.: NN-MLT model prediction for low-latitude region based on artificial neural network and long-term SABER observations. *Earth and Space Science*, *10*, e2023EA002930, https://doi.org/10.1029/2023 EA002930, 2023.

Liu, S-D., and S-S. Liu: *Atmosphere Dynamics*, Peking University Press, Beijing, 2011.

Liu, H. L., Hagan, M. E., & Roble, R. G.: Local mean state changes due to gravity wave breaking modulated by the diurnal tide. *Journal of Geophysical Research*, 105(D10), 12381-12396, (2000).

Liu, H. L., & Hagan, M. E.: Local heating/cooling of Atmospheres. 96(D8), 15297-15309, (1998).

Mlynczak, M. G., Marshall, B. T., Martin-Torres, F. J., Russell III, J. M., Thompson, R. E., Remsberg, E. E., and Gordley, L. L.: Sounding of the Atmosphere using Broadband Emission Radiometry observations of daytime mesospheric O_2 (1Δ) 1.27 μm emission and derivation of ozone, atomic oxygen, and solar and chemical energy deposition rates, 2007.

Meriwether, J. W., and Gerrard, A. J.: Mesosphere inversion layers and stratosphere temperature enhancements, Rev. Geophys., 42, RG3003, http//doi:10.1029/2003RG000133, 2004.

Meriwether, J. W., and Gardner, C. S.: A review of the mesosphere inversion layer phenomenon, J. Geophys. Res., 105, 12 405–12 416, 2000.

Nath, O., & Sridharan, S.: Long-term variabilities and tendencies in zonal mean TIMED–SABER ozone and temperature in the middle atmosphere at 10–15°N. Journal of Atmospheric and Solar-Terrestrial Physics, 120, 1–8, https://doi:10.1016/j.jastp.2014.08.010, 2014.

Ramesh, K., Sridharan, S.: Large mesospheric inversion layer due to breaking of small scale gravity waves: Evidence from Rayleigh lidar observations over Gadanki (13.51^0 N, 79.21^0 E). J. Atmos. Sol. Terr. Phys. 89, 90–97, http://doi.org/10.1016/j.jastp.2012.08.011, 2012.

Ramesh, K., Sridharan, S. and Vijaya Bhaskara, S.: Causative mechanisms for the occurrence of a triple-layered mesospheric inversion event over low latitudes, J. Geophys. Res. Space Physics, 119, 3930–3943, http://doi:10.1002/2013JA019750, 2014.

Ramesh, K., Sridharan, S., Raghunath, K., and Rao, S. V. B.: A chemical perspective of day and night tropical (10°N–15°N) mesospheric inversion layers, J. Geophys. Res. Space Physics, 122, http://doi:10.1002/2016JA023721, 2017.

Ramesh, K., Sridharan, S., Vijaya Bhaskara Rao, S., Raghunath, K., Bhavani Kumar, K.: Rayleigh lidar observations of mesospheric inversion layers over Gadanki (13.5^0N, 79.2^0 E) and their relation with gravity wave activities. Indian Journal of Radio and Space Science, 43, 83-90, 2013.

Remsberg, E., Lingenfelser, V., Harvey, V., Grose, W., Russell III, J., Mlynczak, M., Gordley, L., and Marshall, B. T.: The verification of the quality of SABER temperature, geopotential height, and wind fields by comparison with Met Office assimilated analyses, J. Geophys. Res., 108(D19), 4628, https://doi:10.1029/2003JD003720, 2003.

Rezac, L., Kutepov, A., Russell, J.M., Feofilov, A.G., Yue, J., and Goldberg, R.A.: Simultaneous retrieval of T (p) and CO2 VMR from two-channel non-LTE limb radiances and application to

562 daytime SABER/ TIMED measurements. J. Atmos. Sol. Terr. Phys 130–131, 23–42.
563 https://doi.org/10.1016/j.jastp.2015.05.004, 2015.
564 Russell, J.M., Mlynczak, M.G., Gordley, L.L., Tansock, J., Esplin, R.: An overview of the
565 SABER experiment and preliminary calibration results. In Proceedings of the SPIE, 44th
566 Annual Meeting, Denver, CO, USA, 3756, 277–288, 1999.
567 Schmidlin, F. J.: Temperature inversions near 75 km. *Geophysical Research Letters*, 3(3),
568 173-176, (1976).
569 Sica, R. J., Argall, P. S., Shepherd, T. G., and Koshyk, J. N.: Model-measurement comparison of
570 mesospheric temperature inversions, and a simple theory for their occurrence, Geophys. Res.
571 Lett., 34, L23806, https://doi:10.1029/2007GL030627, 2007.
572 Sivakandan, M., Kapasi, D., and Taori, A.: The occurrence altitudes of middle atmospheric
573 temperature inversions and mesopause over low-latitude Indian sector, Ann. Geophys., 32,
574 967–974, https://doi.org/10.5194/angeo-32-967-2014, 2014.
575 Siva Kumar, V., Bhavani Kumar, Y., Raghunath, K., Rao, P. B., Krishnaiah, M., Mizutani, K.,
576 Aoki, T., Yasui, M., and Itabe, T.: Lidar measurements of mesospheric temperature inversion
577 at a low latitude, Ann. Geophys., 19, 1039–1044, https://doi.org/10.5194/angeo-19-1039-2001,
578 2001.
579 Sridharan, S., Sathishkumar, S., and Gurubaran, S.: Influence of gravity waves and tides on
580 mesospheric temperature inversion layers: simultaneous Rayleigh lidar and MF radar
581 observations, Ann. Geophys., 26, 3731–3739, 2008.
582 Singh, R. P., & Pallamraju, D.: Mesospheric temperature inversions observed in OH and O2
583 rotational temperatures from Mount Abu (24.6°N, 72.8°E), India. Journal of Geophysical
584 Research: Space Physics, 123, 8823–8834, https://doi.org/10.1029/2018JA025703, 2018.
585 Smith, A.: Global Dynamics of the MLT, Surv. Geophys, 33, 1177–1230,
586 https://doi.org/10.1007/ s10712-012-9196-9, 2012.
587 Szewczyk, A., Strelnikov, B., Rapp, M., Strelnikova, I., Baumgarten, G., Kaifler, N., Dunker, T.,
588 and Hoppe, U. P.: Simultaneous observations of a Mesospheric Inversion Layer and turbulence
589 during the ECOMA-2010 rocket campaign, Ann. Geophys., 31, 775–785, http://doi:10.5194/
590 angeo-31-775-2013, 2013.
591 Vadas, S. L., and Fritts, D. C.: Thermosphere responses to gravity waves: Influences of
592 increasing viscosity and thermal diffusivity, J. Geophys. Res., VOL. 110, D15103, doi:
593 10.1029/2004JD 005574, 2005.

Wang, L., Geller, M.A., Alexander, M.J.: Spatial and Temporal Variations of Gravity Wave Parameters. Part I: Intrinsic Frequency, Wavelength, and Vertical Propagation Direction. J. Atmos. Sci., 62, 125–142, http://doi.org/10.1029/2010JD013860, 2005.

Wang, L., and Alexander, M.J.: Global estimates of gravity wave parameters from GPS radio occultation temperature data. J. Geophys.Res. 115, D21122, http://doi.org/10.1029/2010J D013860, 2010.

Walterscheid, R. L., and Hickey, M. P.: Gravity wave ducting in the upper mesosphere and lower thermosphere duct system, J. Geophys. Res., 114, D19109, http://doi:10.1029/2008JD 011269, 2009.

Yuan, T., Pautet, P. D., Zhao, Y., Cai, X., Criddle, N. R., Taylor, M. J., and Pendleton, W. R.: Coordinated investigation of mid-latitude upper mesospheric temperature inversion layers and the associated gravity wave forcing in Logan, Utah, J. Geophys. Res. Atmos., 119, 3756–3769, http://doi:10.1002/2013JD020586, 2014.